Meso-scale Fracture Modelling of Concrete Based on X-ray Computed Tomography Images

Wenyuan Ren[1], *Zhenjun Yang[1,2], and Phil Withers[3]

[1]School of Mechanical, Aerospace and Civil Engineering, the University of Manchester, UK.
[2]College of Civil Engineering and Architecture, Zhejiang University, China.
[3] Manchester X-ray Imaging Facility, School of Materials, the University of Manchester, UK.

*Corresponding author: zhjyang@zju.edu.cn

Abstract

Meso-scale two-dimensional finite element models are developed for fracture modelling in concrete based on images from an in-situ microscale X-ray Computed Tomography test. In the models, the material heterogeneity is characterised by "real" multi-phases, namely, aggregates, cement and voids. Zero-thickness cohesive interface elements (CIEs) with normal/shear traction-separation constitutive laws are embedded within cement and on aggregate-cement interfaces to simulate potential cracks. Simulations of uniaxial tension tests were carried out. The results show good qualitative and quantitative agreement with experimental observations and simulations from literatures.

Keywords: Concrete, X-ray computed tomography, Image based modelling, Cohesive zone model, Meso-scale finite element model

Introduction

Micro/meso-scale modelling of damage and fracture in quasi-brittle multiphase materials, such as concrete and fibre reinforced polymers, has received more and more attention, in order to obtain more accurate understanding of their failure mechanisms and evaluation of uncertainty and reliability due to random distribution of phases. There are basically two approaches in characterising random heterogeneity in materials numerically: direct approach and indirect approach. In the direct approach, different phases including matrices, inclusions and interfaces are explicitly modelled by finite elements (FE) with assigned properties. The randomness in the spatial distribution of different phases is realised by randomised positions and shapes of inclusions (Lilliu and van Mier, 2003; López *et al*., 2008; Skarżyński and Tejchman, 2010; Yin *et al*., 2012). In the indirect approach, the material properties are modelled as spatially-varying random fields with given correlation structures, so different phases are implicitly modelled (Xu, 2007; Xu and Chen, 2009; Yang *et al*., 2009; Su *et al*., 2010). However, most of these studies use assumed micro/meso-scale morphologies or random field properties, which are not direct and accurate representation of the internal structures of the materials. Therefore, the simulated micro/meso-scale damage and fracture processes cannot be directly and accurately validated, although macro-scale load-displacement curves can mostly be obtained.

More representative geometrical models can be constructed based on images obtainable from techniques such as digital cameras (Yue *et al*., 2003) and microscopes (Michailidis *et al*., 2010), and more recently, the X-ray Computed Tomography (XCT). The XCT, routinely used in hospitals, has now become attractive for characterising microstructures of materials, because of its high resolution, non-destructive nature, and clear visualisation. In the last decade, tremendous efforts have been made in applying the XCT to characterise microstructures and study evolutions of damage and fracture of a variety of materials, such as geological materials (rock, soil and fossils)

(Carlson WD, 2006), metals and alloys (Babout *et al*., 2006; Marrow and Babout, 2006; Qian *et al*., 2008), porous materials (Kerckhofs *et al*., 2008), composites (Drummond *et al*., 2005) and concrete (Garboczi, 2002; Wang *et al*., 2003). However, XCT-image based modeling and analysis is only conducted occasionally, for example, by Hollister *et al*. (1994) for trabecular bones, Terada *et al*., (1997) for metal matrix composites, Ali *et al*. (2009) and Sharma *et al*. (2012) for carbon/carbon composites, Mostafavi *et al*. (2013) for polygranular graphite, and Jivkov *et al*. (2013) for concrete, respectively. However, most of these studies carried out linear elastic stress analysis or calculated effective stiffness based on homogenisation method, and XCT image-based modelling of complicated fracture has hardly been conducted.

In this study, meso-scale 2D FE models are developed for fracture modelling in concrete based on images from an in-situ microscale XCT test (Yang *et al*., 2013). In these models, the material heterogeneity is characterised by three phases, namely, aggregates, cement and voids. To model complicated fracture processes, zero-thickness cohesive interface elements (CIEs) with normal/shear traction-separation constitutive laws are embedded within cement and on aggregate-cement interfaces to simulate potential cracks, using an algorithm extended from a previous one for homogeneous materials (Yang *et al*, 2009). Simulations of uniaxial tension tests were carried out. The influence of the inclusions' distribution on overall stress-displacement curves and crack patterns was investigated.

Building of the meso-scale models

Image processing

The segmented 37.2 mm concrete cube from the in-situ XCT test (Yang *et al*., 2013) is shown in Figure 1, highlighting the locations of a few cross-sections to be studied. Figure 2 shows the image of cross-section 1, in which the dark, grey and white regions represent aggregates, cement and voids, respectively. The gray levels in this image are continuous (0-255) and roughly uniform in the regions of each colour. There are 372 pixels in each direction, so each pixel represents 0.1 mm. Before mesh generation, the image is processed into a binary one, by assigning 1 to aggregates and 2 to cement, after it is segmented into three phases using a proper threshold range of gray values for each, specifically, 0-120 for aggregates (dark areas), 121-220 for cement (grey areas) and 221-255 for voids (white areas). To simplify mesh generation, the phase value (1 or 2) of small regions with one pixel width (highlighted by red circles in Figure 2) is changed to be consistent with their surrounding regions. The image after processing is shown in Figure 3.

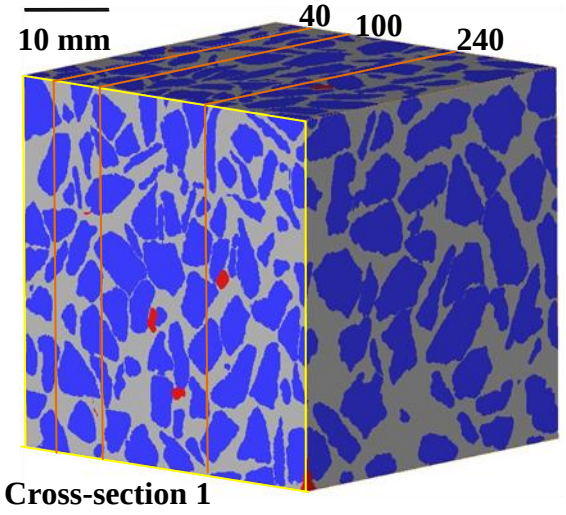

Figure 1. The segmented concrete cube

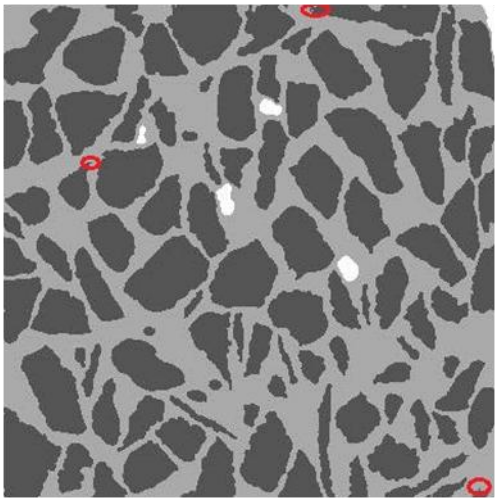

Figure 2. The image of cross-section 1

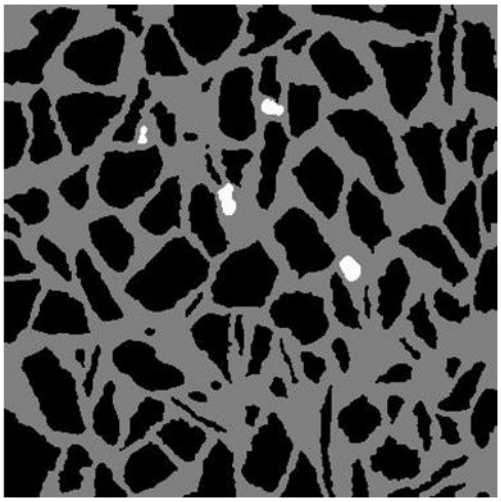

Figure 3. After image processing

Initial mesh generation

The binary image in Figure 3 consists of an array of square pixels. Figure 4a shows a small part of Figure 3. Naturally, each pixel can be modelled by a quadrilateral element in the FE mesh. The resultant mesh is shown in Figure 4b, in which the boundaries between two phases are zigzagged. This situation is caused by image resolution and may not represent the real material interfaces. In addition, the stress concentration at the corner points may lead to numerical difficulties in FE simulations. Therefore, these inter-phase boundaries are further smoothed by dividing the corner elements into two triangles and assigning proper phase values. The smoothed mesh is shown in Figure 4c.

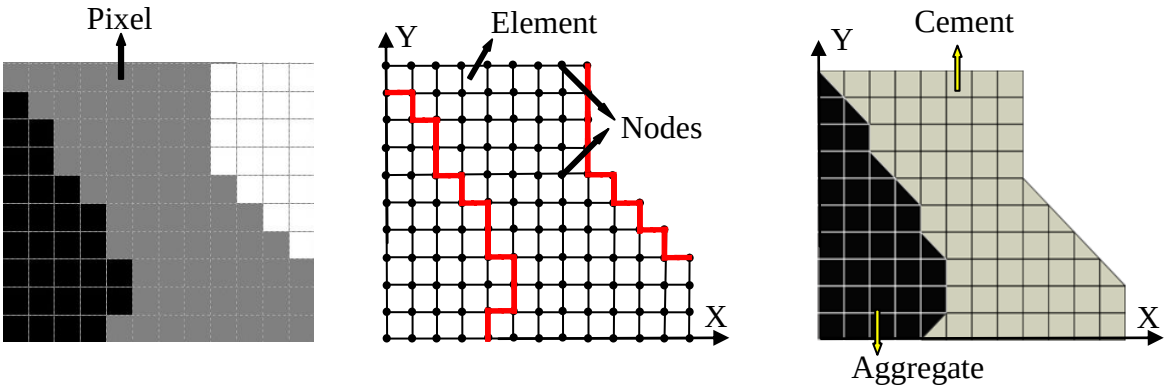

(a) Image **(b) Grid mesh** **(c) Smoothed mesh**

Figure 4. Transformation from pixel to mesh grid

Cohesive interface elements insertion

In order to simulate realistic fracture processes, four-noded cohesive interface elements (CIEs) with zero in-plane thickness are inserted into the generated initial mesh. The detailed CIE insertion procedure devised for homogeneous materials in (Yang *et al.*, 2009) is extended to account for multi-phases and interfaces. Three sets of CIEs with different traction-separation softening laws are inserted, namely, CIE_AGG inside the aggregates, CIE_CEM inside the cement, and CIE_INT on the aggregate-cement interfaces. As the aggregates have much higher strength than the cement and the interfaces, no cracks are allowed to initiate inside the aggregates by assuming elastic behaviour without damage to CIE_AGG.

The final FE mesh after the insertion of CIEs based on the XCT image in Figure 3 is shown in Figure 5. It has 357,324 nodes and 291,875 elements including 141,505 solid elements and 150,370 CIEs. The CIE_INT elements are highlighted as red lines.

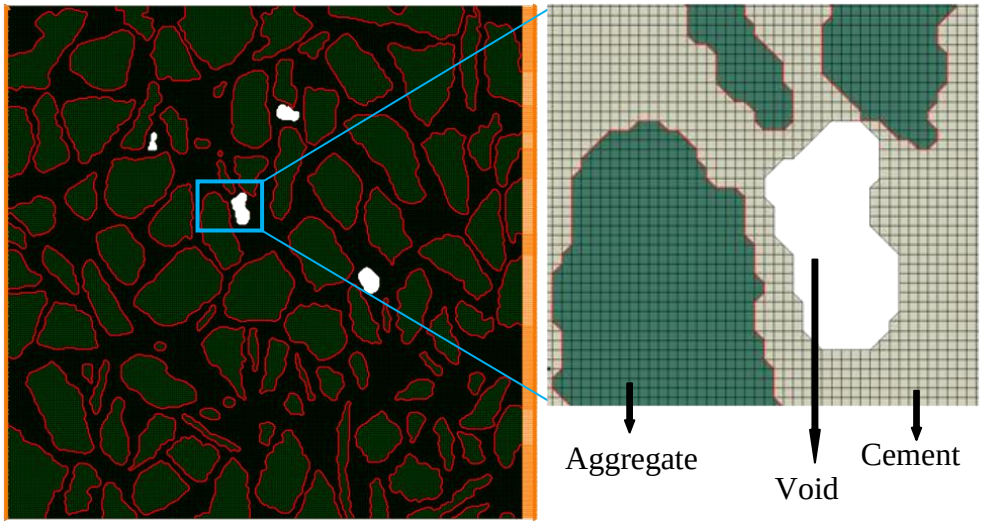

Figure 5. The FE mesh based on the XCT image in Figure 2

Numerical simulations of uniaxial tension test

Model parameters

The aggregates and cement are assumed to behave linear elastically. The linear tension/shear softening laws are used to model CIEs (Yang *et al*., 2009) with quadratic nominal stress initiation criterion and linear damage evolution criterion. For comparison of results, the same material properties as used in (López *et al*., 2008) are used in this study. They are listed in Table 1. Due to the lack of experimental data, the shear fracture properties are assumed to be the same as the normal ones.

Uniaxial tension tests are simulated. The image-based models are fixed at the left boundary and are subjected to a uniformly distributed displacement at the right boundary, i.e., a displacement-controlled loading scheme is used. All analyses are ended at a displacement d=0.2mm. The Abaqus/Explicit is used to solve the nonlinear equation systems with a step time of 0.01s, which is found long enough to ensure the quasi-static loading condition.

Table 1. Material properties

	Elastic modulus (GPa)	Poisson's ratio	Density (10^{-9} tone/mm^3)	Elastic stiffness (MPa/mm)	Tensile strength (MPa)	Fracture energy (N/mm)
Aggregate	70	0.2	2.5	/	/	/
Cement	25	0.2	2.2	/	/	/
CIE_AGG	/	/	2.5	10^6	/	/
CIE_CEM	/	/	2.2	10^6	6	0.06
CIE_INT	/	/	2.2	10^6	3	0.03

Typical Results

The average stress (σ) –displacement (d) curve is plotted in Figure 6, together with the experimental curve (Hordijk, 1992) and the simulation results from an assumed meso-structure (López *et al*., 2008). The average stress σ is calculated by dividing the total nodal reaction force of all the nodes on the left boundary by the specimen cross-section area. It can be seen that the peak loads and the post-peak parts of three curves are close. However, one should not intend to compare the curves in Figure 6 directly, as they are responses of specimens of very different sizes. A direct comparison of the present simulation with the in-situ XCT test (Yang *et al*., 2013) is not available because the specimen is under compression rather than tension in the test.

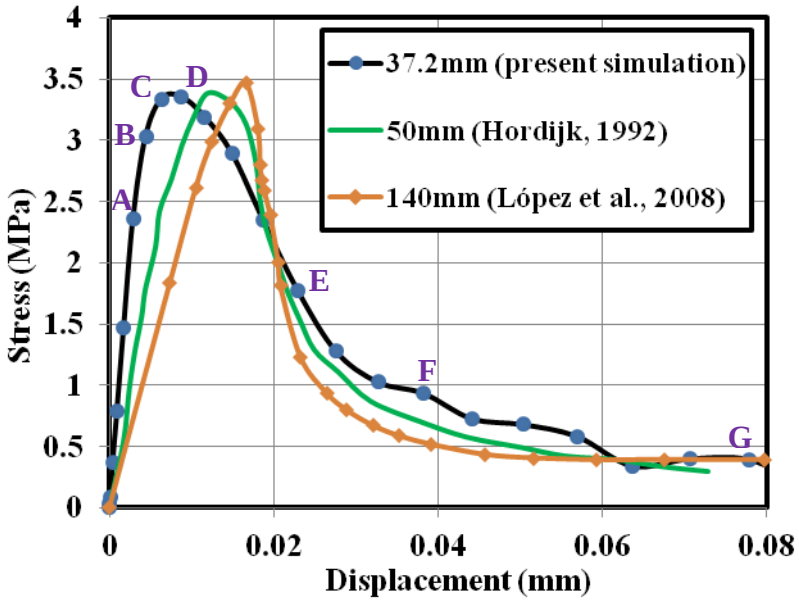

Figure 6. Average stress-displacement curves under uniaxial tension

Figure 7 illustrates the propagation of microcracks before the peak load, which are represented by the CIEs with scalar damage index (SDEG in ABAQUS) over 0.9. It should be noted that SDEG=1.0 means complete failure. All the predicted crack figures in this paper are shown using a displacement scale factor (DSF) =10. A few microcracks initiate on the aggregate-cement interfaces at low stress σ=2.36 MPa (Figure 7a). More and more microcracks appear as the stress increases. At the end of the elastic behaviour stage at σ=3.03 MPa at Point B in Figure 6, the microcrack pattern already looks complicated (Figure 7b). A crack pattern in the nonlinear stage (σ=3.34 MPa at Point C) is shown in Figure 7c, which looks similar to that at the peak point D with σ=3.36 MPa in Figure 7d. The predicted scenario in Figure 7 indicates that a large number of microcracks initiate very quickly at the early loading stage, and the crack pattern becomes gradually stable in the pre-peak nonlinear stage. It can also be seen that before the peak load is reached, the microcracks are not connected to form any dominant macrocracks. This is because most of them are on the aggregate-cement interfaces due to the relative low tensile strength (3MPa), and only a small number of them are inside the cement due to its high tensile strength (6MPa). It is also reconfirmed that the approach of pre-embedding CIEs is very flexible and powerful in modelling complicated fracture process.

The predicted post-peak crack propagation process is illustrated in Figure 8, in which the different phases are shown. It can be seen that at the peak load, there is still no evident macrocracks (Figure 8a). As the displacement increases, some aggregate-cement interfacial cracks continue to propagate and are gradually connected by newly formed cracks in the cement phase (Figure 8b and 8c). The

specimen fails with two main macrocracks (Figure 8d). It should be noted that the microcracks in Figure 7 still exist, but they are not shown in Figure 8 because their width is much smaller than that of the two macrocracks.

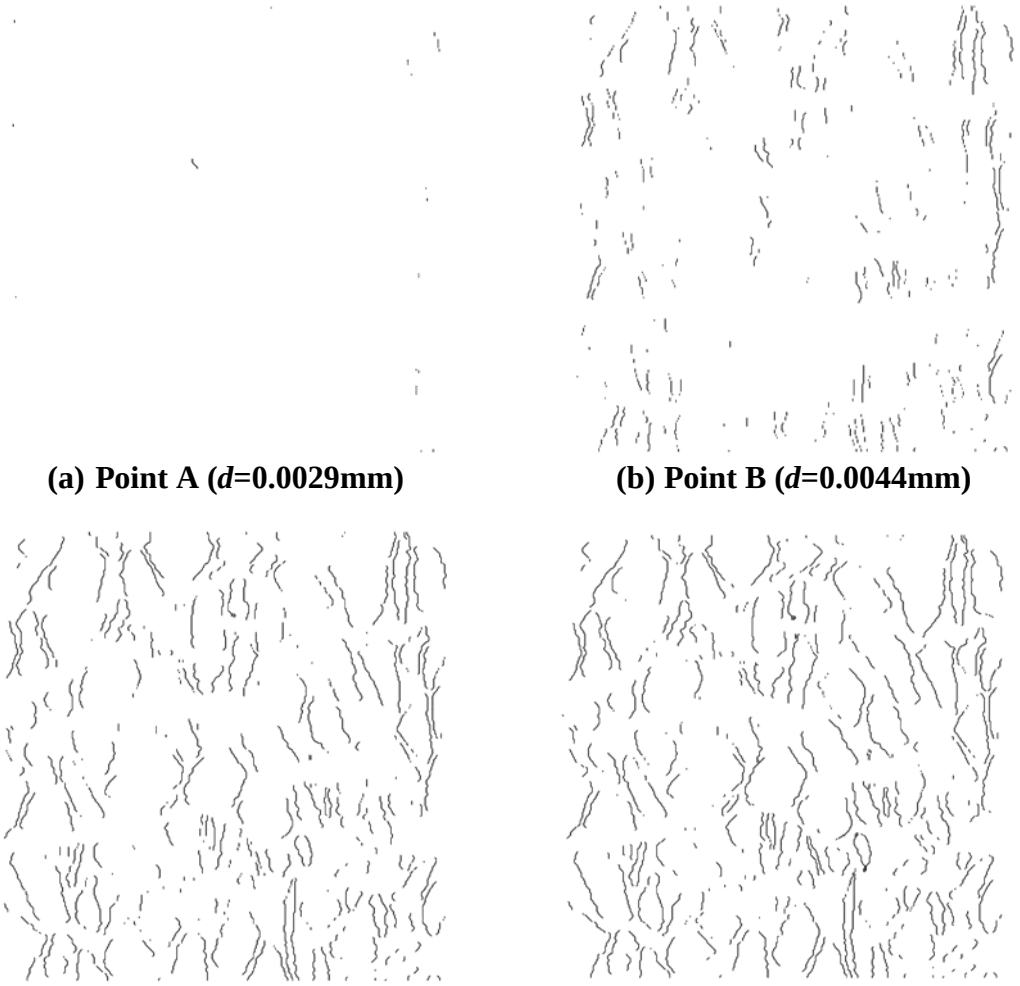

(a) Point A (*d*=0.0029mm) **(b) Point B (*d*=0.0044mm)**

(c) Point C (*d*=0.0064mm) **(d) Point D (*d*=0.0087mm)**

Figure 7. The pre-peak microcracking process

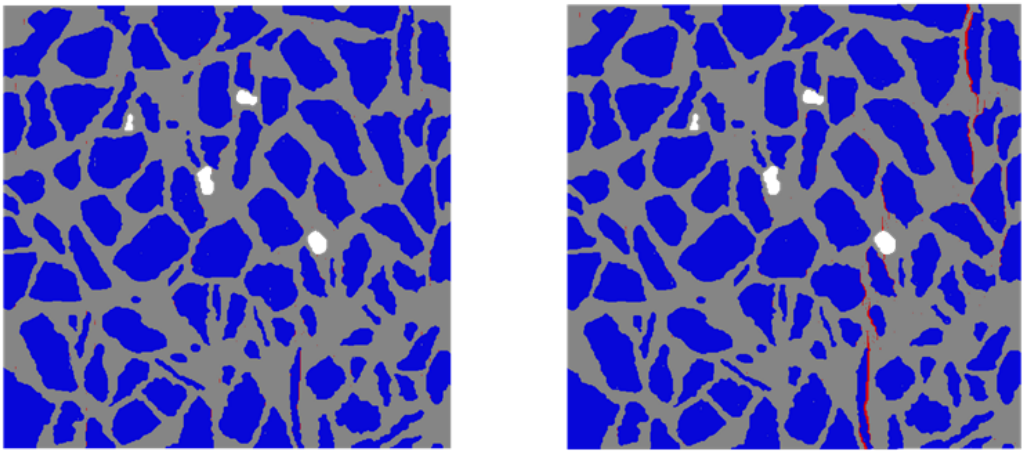

(a) Point D (*d*=0.0087mm) **(b) Point E (*d*=0.0229mm)**

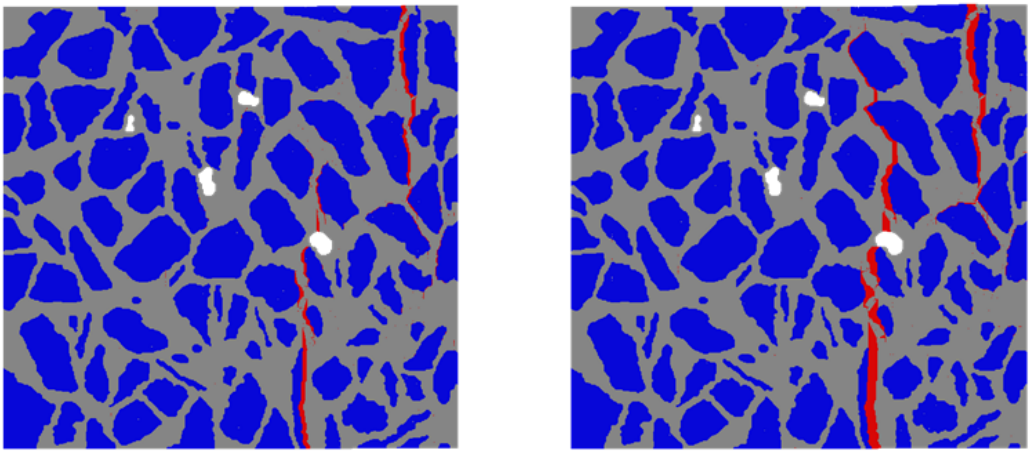

(c) Point F (*d*=0.0382mm) **(d) Point G (*d*=0.0778mm)**

Figure 8. The macrocrack propagation process

Effects of loading direction

The same model in Figure 5 is simulated under uniaxial tension in the vertical (Y) direction. The predicted average stress - displacement curves are shown in Figure 9. It can be seen that the predicted strengths of the same specimen differ about 11% (3.4MPa and 3.8MPa). A different crack pattern from Figure 8d is predicted, as shown in Figure 10. These differences are caused by different loading directions, or equivalently, by different distributions of phases of the same volume fractions under the same loading direction. The pre-peak elastic parts of the two curves in Figure 10 are identical and independent of the phase distribution, which has also been noticed in (Skarżyński and Tejchman, 2010) and (Yin *et al*., 2013).

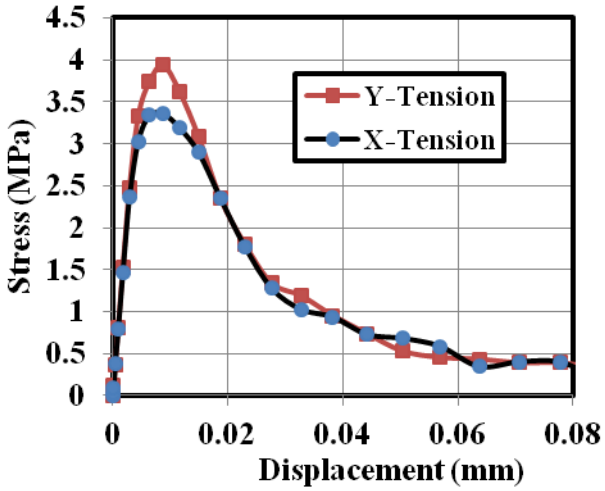

Figure 9. Average stress-displacement curves under different tension directions

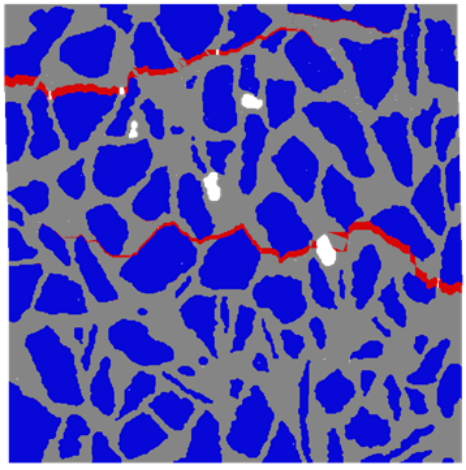

Figure 10. Crack pattern under vertical tension (*d*=0.0778mm)

Effects of image location

Three more images on different cross-sections along another direction (shown in Figure 1) are transformed into 2D FE models which are simulated under uniaxial tension. The average stress - displacement curves are compared in Figure 11, with the final crack patterns shown in Figure 12-14 for the cross-section 40, 100 and 240, respectively. The very different load-carrying capacities and crack patterns at different locations in the same specimen reflect the effects of random distribution of phases of random shapes and sizes. This also demonstrates the limitations of 2D meso-scale

modelling and the necessity of 3D modelling, as there exists only one crack pattern in the physical test of one specimen.

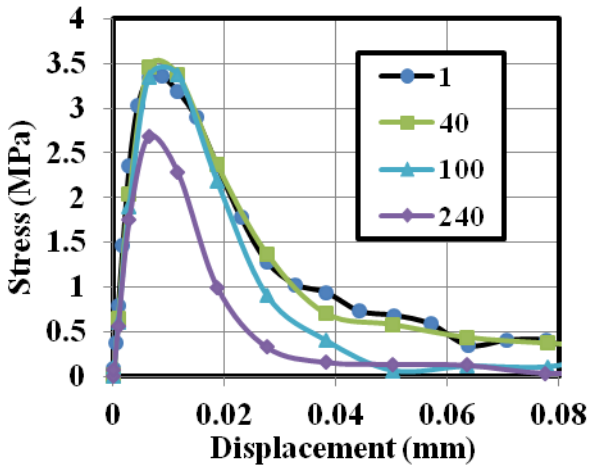

Figure 11. Average stress-displacement curves from different images

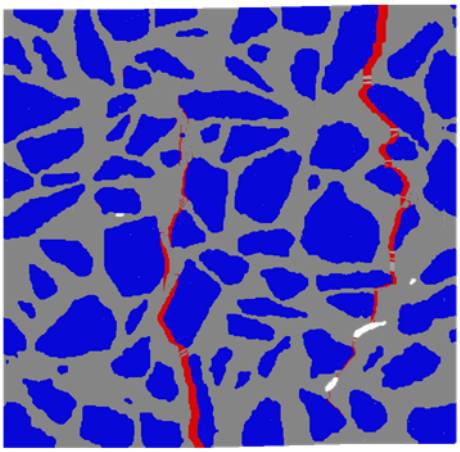

Figure 12. Crack pattern of cross-section 40 (*d*=0.0778mm)

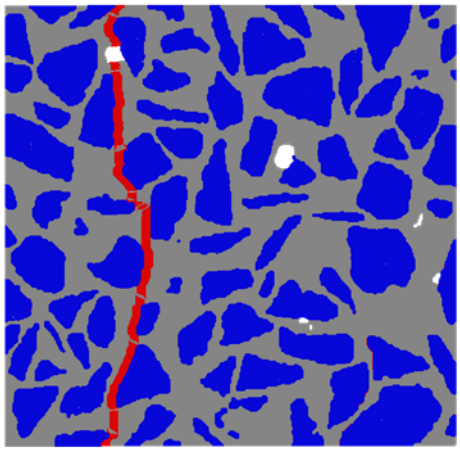

Figure 13. Crack pattern of cross-section 100 (*d*=0.0779mm)

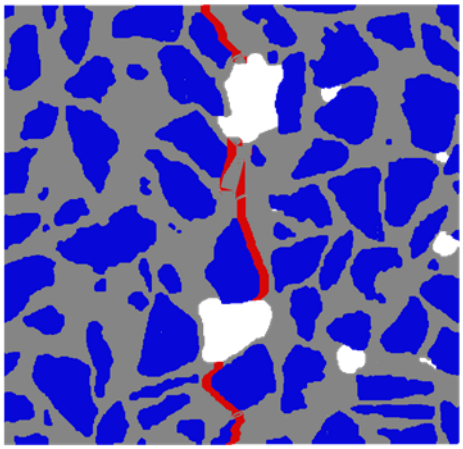

Figure 14. Crack pattern of cross-section 240 (*d*=0.0775mm)

Conclusions

2D meso-scale FE models based on XCT images and the method of pre-embedding cohesive interface elements are built to simulate crack propagation processes in concrete under uniaxial tension loading. The flexibility and effectiveness of pre-embedding CIE technique in modelling realistic, complicated fracture processes is reconfirmed by good qualitative and quantitative agreement of predicted results with experimental observations and simulations from literatures. The very different crack patterns and load-carrying capacities on different cross-sections of the same specimen demonstrate not only the effects of random distribution of phases, but also the limitations of 2D modelling and the necessity of 3D modelling which is currently under way.

Acknowledgement

The research is funded by a Royal Society Research Grant and an EPSRC grant (No. EP/J019763/1). Ren's PhD study in UoM is partially funded by China Scholarship Council. Yang would like to thank the Alexander von Humboldt Foundation, Germany for a Fellowship for Experienced Researchers.

References

Ali, J., Farooqi J. K., Buckthorpe D., Cheyne A. and Mummery P., (2009), Comparative study of predictive FE methods for mechanical properties of nuclear composites. *Journal of Nuclear Materials*, 383(3): 247-253.

Babout, L., Marrow T.J., Engelberg D. and Withers P.J., (2006), X-ray microtomographic observation of intergranular stress corrosion cracking in sensitised austenitic stainless steel. *Materials Science and Technology*, 22(9):1068-1075.

Carlson, W.D., (2006), Three-dimensional imaging of earth and planetary materials. *Earth and Planetary Science Letters*, 249(3-4):133-147.

Drummond, J.L., De Carlo F and Super B.J., (2005), Three-dimensional tomography of composite fracture surfaces. *Journal of Biomedical Materials Research Part B-Applied Biomaterials*, 74B(2):669-675.

Garboczi, E.J., (2002), Three-dimensional mathematical analysis of particle shape using X-ray tomography and spherical harmonics: Application to aggregates used in concrete. *Cement and Concrete Research*, 32(10): 1621-1638.

Hollister, S.J., Brennan J.M. and Kikuchi N., (1994), A homogenization sampling procedure for calculating trabecular bone effective stiffness and tissue level stress. *Journal of Biomechanics* 27(4): 433-444.

Hordijk, D.A. (1992). Tensile and tensile fatigue behaviour of concrete; experiments, modelling and analyses. *Heron*, 37(1): 1-79.

Jivkov, A.P., Engelberg D.L., Stein R. and Petkovski M., (2013), Pore space and brittle damage evolution in concrete. *Engineering Fracture Mechanics*, In Press. DOI: http://dx.doi.org/10.1016/j.engfracmech.2013.05.007.

Kerckhofs, G., Schrooten J., Cleynenvreuqel T., Lomov S.V. and Wevers M., (2008), Validation of x-ray microfocus computed tomography as an imaging tool for porous structures. *Review of Scientific Instruments*, 79(1): Paper No. 013711.

Lilliu, G. and van Mier J. G. M., (2003), 3D lattice type fracture model for concrete. *Engineering Fracture Mechanics*, 70(7–8): 927-941.

López, C., Carol I. and Aguado A., (2008), Meso-structural study of concrete fracture using interface elements. I: numerical model and tensile behavior. *Materials and Structures*, 41(3): 583-599.

Marrow, T.J., Babout L., Jivkov A.P., Wood P., Engelberg D., Stevens N., Withers P.J. and Newman R.C., (2006), Three dimensional observations and modelling of intergranular stress corrosion cracking in austenitic stainless steel. *Journal of Nuclear Materials*, 352(1-3):62-74.

Michailidis, N., Stergioudi F., Omar H. and Tsipas D. N., (2010), An image-based reconstruction of the 3D geometry of an Al open-cell foam and FEM modeling of the material response. *Mechanics of Materials* 42(2): 142-147.

Mostafavi, M., Baimpas N., Tarleton E., Atwood R.C., McDonald S.A., Korsunsky A.M. and Marrow T.J., (2013), Three-dimensional crack observation, quantification and simulation in a quasi-brittle material. *Acta Materialia*. 61(16): 6276-6289.

Qian, L., Toda H., Uesugi K., Ohgaki T., Kobayashi M. and Kobayashi T., (2008), Three-dimensional visualization of ductile fracture in an Al-Si alloy by high-resolution synchrotron X-ray microtomography. *Materials Science and Engineering A-Structural Materials Properties Microstructure and Processing*, 483:293-296.

Sharma, R., Mahajan P. and Mittal R.K., (2012), Fiber bundle push-out test and image-based finite element simulation for 3D *carbon/carbon composites*. Carbon 50(8): 2717-2725.

Skarżyński, Ł. and Tejchman J., (2010), Calculations of fracture process zones on meso-scale in notched concrete beams subjected to three-point bending. *European Journal of Mechanics - A/Solids*, 29(4): 746-760.

Su, X.T., Yang Z.J. and Liu G.H., (2010), Monte Carlo simulation of complex cohesive fracture in random heterogeneous quasi-brittle materials: A 3D study. *International Journal of Solids and Structures*, 47:2336-2345.

Terada, K., Miura T. and Kikuchi N., (1997), Digital image-based modelling applied to the homogenization analysis of composite materials. *Computational Mechanics*, 20(4): 331-346.

Wang, L.B., Frost J.D. and Voyjadjis G.Z., (2003), Quantification of damage parameters using X-ray tomography images. *Mechanics of Materials*, 35: 777-790.

Xu, X.F., (2007), A multiscale stochastic finite element method on elliptic problems involving uncertainties. *Computer Methods in Applied Mechanics and Engineering*, 196, 2723–2736.

Xu, X.F. and Chen X., (2009), Stochastic homogenization of random elastic multi-phase composites and size quantification of representative volume element. *Mechanics of Materials*, 41-2, 174-186

Yang, Z.J., Ren W.Y., Mostafavi M., Mcdonald S. A. and Marrow T. J., (2013), Characterisation of 3D fracture evolution in concrete using in-situ x-ray computed tomography testing and digital volume correlation. *VIII International Conference on Fracture Mechanics of Concrete and Concrete Structures*, Toledo, Spain, CIMNE.

Yang, Z.J., Su X.T., Chen J.F. and Liu G.H., (2009), Monte Carlo simulation of complex cohesive fracture in random heterogeneous quasi-brittle materials. *International Journal of Solids and Structures*, 46(17): 3222-3234.

Yin, A.Y., Yang X.H., Gao H. and Zhu H.P., (2012), Tensile fracture simulation of random heterogeneous asphalt mixture with cohesive crack model. *Engineering Fracture Mechanics*, 92(0): 40-55.

Yin, A.Y., Yang X.H. and Yang Z.J., (2013), 2D and 3D Fracture Modeling of Asphalt Mixture with Randomly Distributed Aggregates and Embedded Cohesive Cracks. *Procedia IUTAM* 6(0): 114-122.
Yue, Z.Q., Chen S. and Tham L.G., (2003), Finite element modeling of geomaterials using digital image processing. *Computers and Geotechnics* 30(5): 375-397.